Supporting Information:

Atomistic Simulations Reveal Structural Disorder in the RAP74-FCP1 Complex

*Christopher Wostenberg,† Sushant Kumar,‡ W. G. Noid† and Scott A. Showalter†**

†Department of Chemistry, The Pennsylvania State University, 104 Chemistry Building, University Park, PA 16802, USA

‡ Huck Insitutes for the Life Sciences, The Pennsylvania State University

cww140@psu.edu (Christopher Wostenberg), suk211@psu.edu (Sushant Kumar), wgn1@psu.edu (W. G. Noid), sas76@psu.edu (Scott A. Showalter)

Supporting Information Summary

Atomistic MD simulations reveal that binding FCP1 impacts the stability and structural organization of RAP74 and also provide new insight into the conformational flexibility of FCP1 in this complex. Supporting Table 1 and Supporting Figures 1-4 provide extended analysis of the interaction of FCP1 residues Leu953 and Leu957 with their respective binding pockets in the FCP1 groove of RAP74. Included are analysis of residues Leu960 and Met961, which serve as controls to demonstrate the extent of solvent access and conformational transitions available to residues that do not make spatio-temporally stable contact with RAP74 The remainder of this supporting information section provides further quantitative characterization of the impact FCP1-RAP74 interactions have on the structure and dynamics of RAP74.

Supporting Information Methods

Secondary Structure definitions

RAP74 subunit is a winged helix domain protein consisting of 4 helices – H1 (Thr455 to Lys466), H2 (Thr469 to Lys475); H2.5 (Gln478 to Gly483); and H3 (Ser485 to Asn501) – and 3 strands – S1 (Pro467 to Met468); S2 (Glu503 to Ile507); and S3 (Lys510 to Ser514). The N- and C- termini of H1, H2, H2.5, S2, and S3 were defined by the first and last amino acids listed above, respectively. However, the N- and C-termini of H3 were defined by the midpoint of the alpha carbons for the first two (Ser485 and Ser486) and last two (Leu500 and Asn501) residues, respectively. These termini were used to calculate the end-to-end distance of each secondary structure and also the distances between different secondary structures.

Helix Dipole Calculation

A backbone dipole was defined for each residue by the backbone atoms - N, CA, H, HA and O. Because the AMBER force field defines a net charge for this atomic group, the backbone dipole moment was calculated after modifying the atomic charges by applying a uniform charge to neutralize the atomic group. We emphasize that these modified charges were only used for analysis purposes and not for the reported simulations. For each secondary structure element, a dipole vector was calculated by summing the dipoles for the corresponding residues.

Helix Orientation and Twist Vectors

The local axis director for each residue was calculated using the g_helixorient utility in the GROMACS software package. For each helix, the principal axis was defined by the vector sum of local axis directors for the corresponding residues. For each strand, the twist vector was similarly calculated as the analogous vector sum. In particular, the local twist vector for the ith residue was defined by the cross product of the displacement vector between residue i-1 and residue i+1 and the displacement vector between residue i and residue i+2.

Table 1: Molecular Dynamics Determined Average Distances for Key Intermolecular Interactions

RAP74 Residue and Atom	FCP1 Residue and Atom	Average Distance (Å)	Percent Less Than 4.0 Å
Thr470 C_{γ}	Leu953 $C_{\delta1}$	5.83	0.9
Thr470 C_{γ}	Leu953 $C_{\delta2}$	4.24	33.4
Thr470 $O_{\gamma1}$	Glu954 $O_{\varepsilon1}$	5.48	14.2
Thr470 $O_{\gamma1}$	Glu954 $O_{\varepsilon2}$	5.53	14.5
Lys471 N_{ζ}	Asp947 $O_{\delta1}$	4.77	32.9
Lys471 N_{ζ}	Asp947 $O_{\delta2}$	4.68	34.1
Leu474 $C_{\delta1}$	Met949 C_{ε}	6.35	2.7
Leu474 $C_{\delta2}$	Met949 C_{ε}	5.74	7.4
Leu474 $C_{\delta1}$	Leu953 $C_{\delta1}$	5.95	0.4
Leu474 $C_{\delta1}$	Leu953 $C_{\delta2}$	4.84	14.4
Leu474 $C_{\delta2}$	Leu953 $C_{\delta1}$	6.16	0.3
Leu474 $C_{\delta2}$	Leu953 $C_{\delta2}$	5.04	4.0
Ser486 C_{β}	Met949 C_{ε}	4.53	29.0
Val490 $C_{\gamma1}$	Met949 C_{ε}	6.28	5.6
Val490 $C_{\gamma2}$	Met949 C_{ε}	6.21	5.4
Asn491 $N_{\delta1}$	Glu956 $O_{\varepsilon1}$	4.74	38.7
Asn491 $N_{\delta1}$	Glu956 $O_{\varepsilon2}$	4.73	38.7
Leu493 $C_{\delta1}$	Leu953 $C_{\delta1}$	5.67	0.2
Leu493 $C_{\delta1}$	Leu953 $C_{\delta2}$	5.71	2.0
Leu493 $C_{\delta2}$	Leu953 $C_{\delta1}$	4.59	16.3
Leu493 $C_{\delta2}$	Leu953 $C_{\delta2}$	4.28	44.5
Leu497 $C_{\delta1}$	Leu957 $C_{\delta1}$	4.72	16.4
Leu497 $C_{\delta1}$	Leu957 $C_{\delta2}$	4.75	13.2
Leu497 $C_{\delta2}$	Leu957 $C_{\delta1}$	5.73	3.2
Leu497 $C_{\delta2}$	Leu957 $C_{\delta2}$	5.77	4.3
Lys498 N_{ζ}	Asp959 $O_{\delta1}$	6.63	14.7
Lys498 N_{ζ}	Asp959 $O_{\delta2}$	6.53	17.4
Phe513 C_{ζ}	Leu957 $C_{\delta1}$	5.07	20.6
Phe513 C_{ζ}	Leu957 $C_{\delta2}$	4.58	36.0

Interactions Stabilizing the RAP74-FCP1 Complex

In the main text we describe the extensive dynamics of Met949 in the shallow FCP1 binding groove on the surface of RAP74. Here we provide additional figures documenting the relative structural disorder of Leu953 and Leu957, which are the other two hydrophobic FCP1 residues defining the non-polar RAP74/FCP1 interface. Additional analysis is provided of Leu960 and Met961, which are solvent exposed, as a comparison that establishes a frame of reference for the extent of conformational restriction and exclusion from solvent experienced by the three residued providing critical interactions.

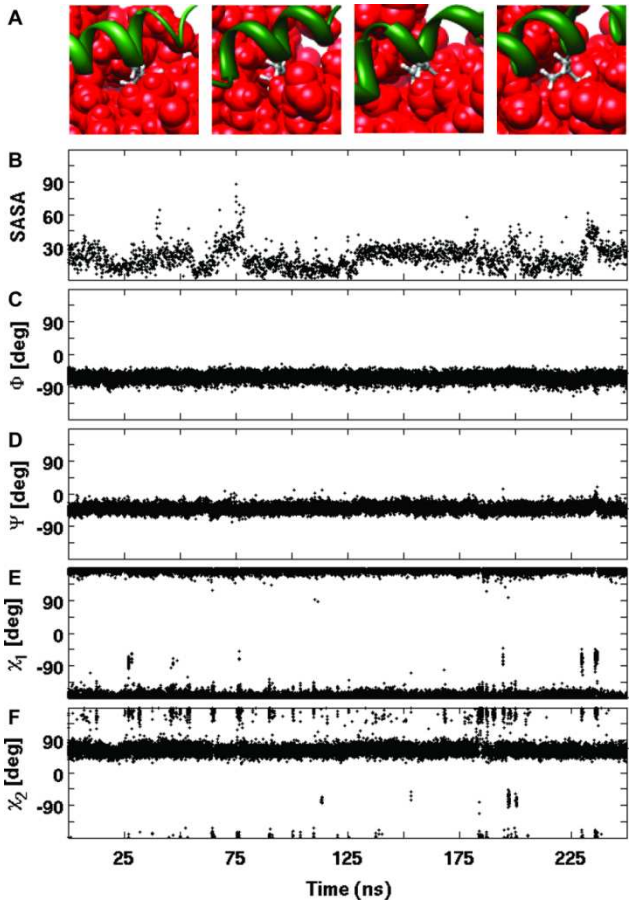

Figure S1: The sidechain of Leu953 is held tightly in the RAP74 binding groove. (A) Representative snapshots taken at 50 ns, 100 ns, 150 ns, and 200 ns zoomed in to show Leu953 (colored by atom) from FCP1 (green ribbon) bound to the RAP74 binding groove (red van der Waals spheres). (B) Solvent accessible surface area of Leu953 as a function of time. The remaining panels display Leu953 torsion angles φ (C), ψ (D), χ_1 (E), and χ_2 (F) as a function of time.

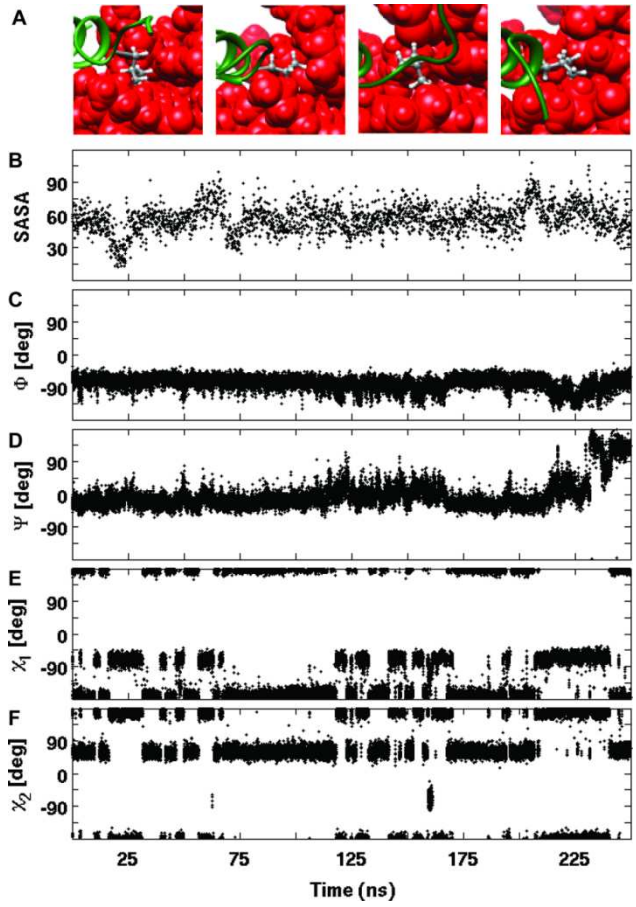

Figure S2: The sidechain of Leu957 undergoes significant conformational dynamics, but does not escape from the RAP74 binding groove during the course of the simulation. (A) Representative snapshots taken at 50 ns, 100 ns, 150 ns, and 200 ns zoomed in to show Leu957 (colored by atom) from FCP1 (green ribbon) bound to the RAP74 binding groove (red van der Waals spheres). (B) Solvent accessible surface area of Leu957 as a function of time. The remaining panels display Leu957 torsion angles φ (C), ψ (D), χ_1 (E), and χ_2 (F) as a function of time. Backbone torsion angles φ and ψ show the melting out of helical structure in the final 50 ns of the semulation, although this transition does not result in release of the Leu957 sidechain from the binding groove.

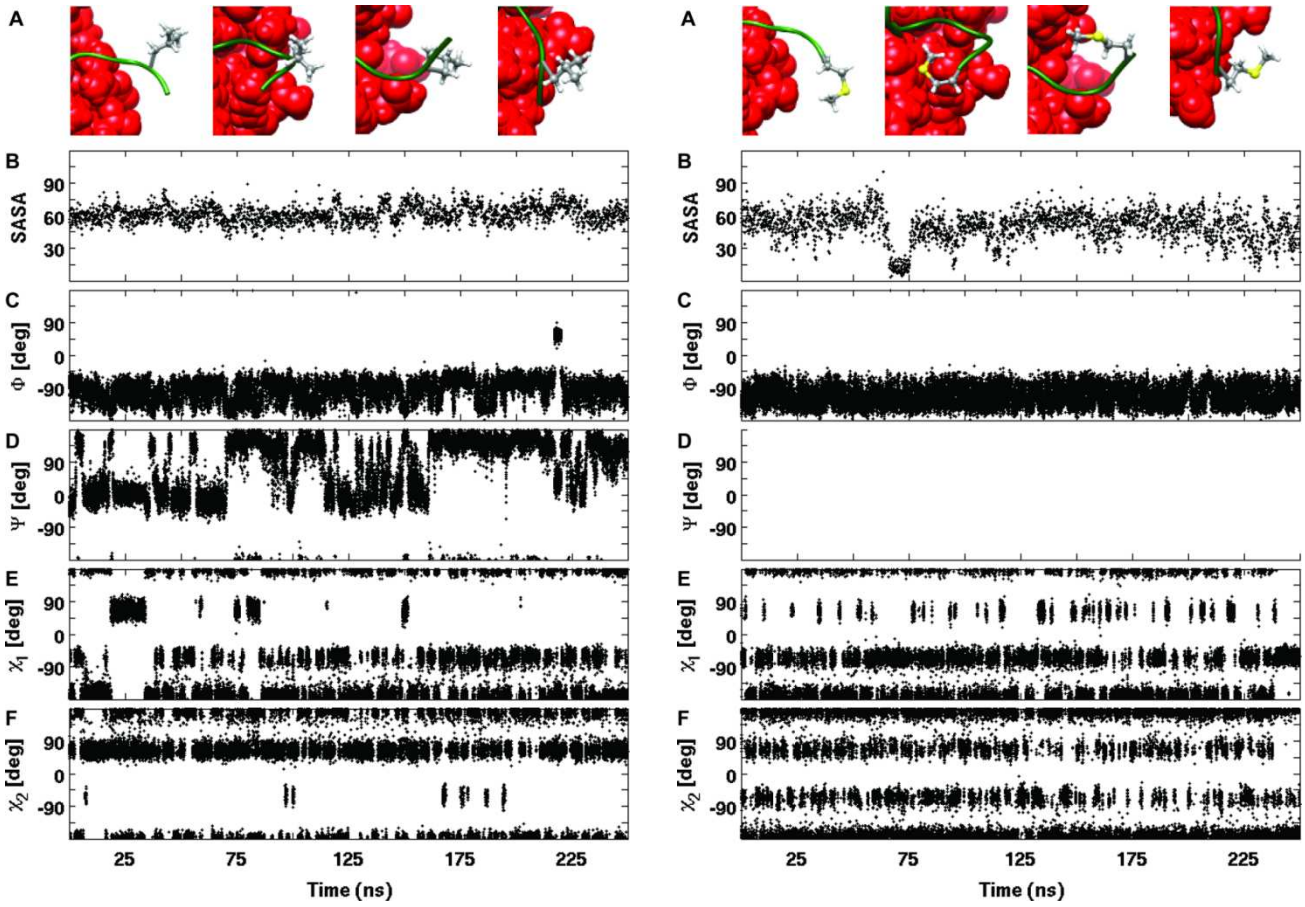

Figure S3 (left): The sidechain of Leu960 is representative of a Leu sidechain that does not make strong interactions with RAP74. (A) Representative snapshots taken at 50 ns, 100 ns, 150 ns, and 200 ns zoomed in to show Leu960 (colored by atom) from FCP1 (green ribbon) and RAP74 (red van der Waals spheres). (B) Solvent accessible surface area of Leu960 as a function of time. The remaining panels display Leu960 torsion angles φ (C), ψ (D), χ_1 (E), and χ_2 (F) as a function of time.

Figure S4 (right): The sidechain of Met961 is representative of a Met sidechain that does not make strong interactions with RAP74. (A) Representative snapshots taken at 50 ns, 100 ns, 150 ns, and 200 ns zoomed in to show Met961 (colored by atom) from FCP1 (green ribbon) and RAP74 (red van der Waals spheres). (B) Solvent accessible surface area of Met961 as a function of time. The remaining panels display Met961 torsion angles φ (C), ψ (D), χ_1 (E), and χ_2 (F) as a function of time.

FCP1 alters RAP74 structure and dynamics

Atomistic MD simulations reveal that binding FCP1 impacts the stability and structural organization of RAP74 and also provide new insight into the conformational flexibility of FCP1 in this complex. This supporting information section provides further quantitative characterization of the impact FCP1-RAP74 interactions have on the structure and dynamics of RAP74. Supporting Figure 5 indicates that RAP74 accommodates FCP1 by exposing key residues in the hydrophobic groove, while also withdrawing residues on the exterior of this pocket. Supporting Figure 6 demonstrates that the FCP1 helix dipole tends to partially align with the H2 helix and anti-align with H3. Supporting Figure 7 demonstrates that this interaction does not significantly alter the structure or orientation of H2. Supporting Figure 8 demonstrates that, upon binding FCP1, the hydrophobic groove of RAP74 expands and become more stable. Supporting Figures 9 and 10 suggest that, after binding FCP1, H2.5 helix approaches H3 at a right angle while aligning more closely with H2. Supporting Figure 11 demonstrates that, after binding FCP1, H1 becomes more compact and aligns at an increasingly anti-parallel orientation with respect to H2. Supporting Figure 12 indicates that FCP1 stabilizes the alignment of strands S2 and S3. Supporting Figures 13 and 14 demonstrate that the RAP74 binding pocket stabilizes the helical axis of FCP1, especially near the N-terminal of FCP1, while the C-terminal samples larger and more correlated fluctuations along its axis. Supporting Figure 15 suggests that hydrophobic interactions involving Ala946 and Ala950 stabilize the N-terminal turn of FCP1 until the last 10ns. In contrast, Supporting Figure 16 demonstrates that contacts involving Met949-Leu953 and Leu953-Leu957 remain very stable and anchor the C-terminal turn of FCP1. Supporting Figure 17 demonstrates that the FCP1 dipole samples significant fluctuations and rapidly decays during the last 50ns of the simulation.

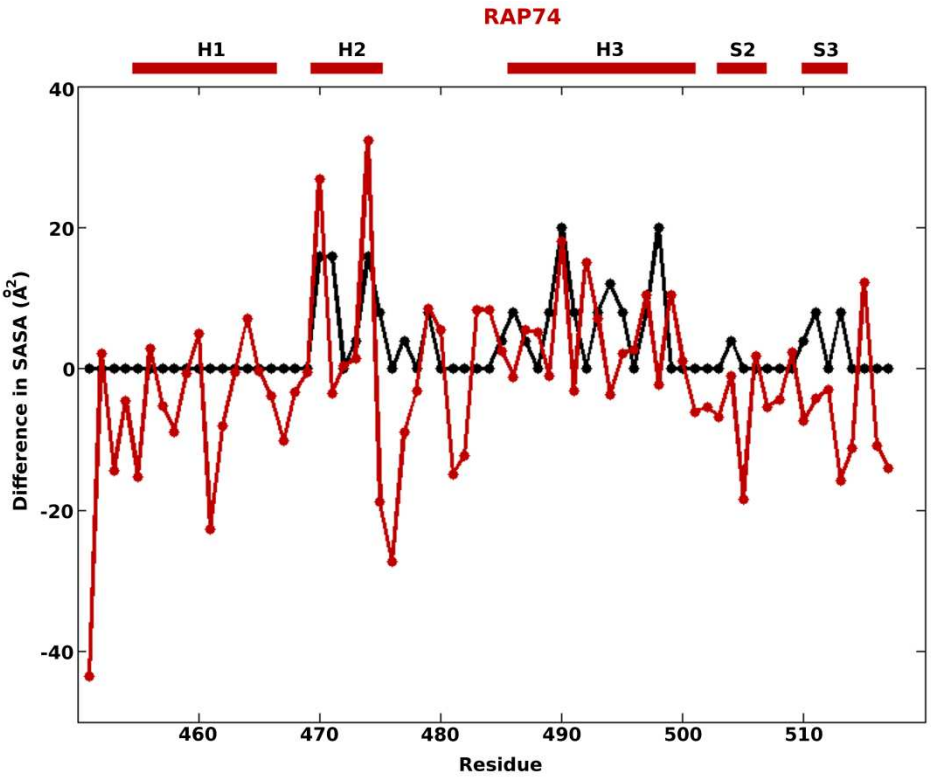

Figure S5: Changes in Accessible Surface Area (ASA) of RAP74 upon binding FCP1. The black curve identifies the regions of RAP74 that are in direct contact with FCP1 by presenting the number of intermolecular contacts formed by each residue in the crystal structure. (The data in the black curve has been multiplied by a factor of four so that both curves fit on the same scale.) The red curve presents the difference in per-residue Accessible Surface Area (ASA) between holo and apo RAP74 and shows that RAP74 residues directly contacting FCP1 become more surface exposed (to either solvent or FCP1) in the complex. Reorganization of RAP74 also results in a significant number of residues becoming increasingly buried (negative difference), meaning that they are less accessible to both solvent and FCP1; these residues are almost never in direct contact with FCP1. Of particular note is H1, which tilts to become increasingly antiparallel with H2, resulting in an oscillatory set of changes in per-residue surface exposure.

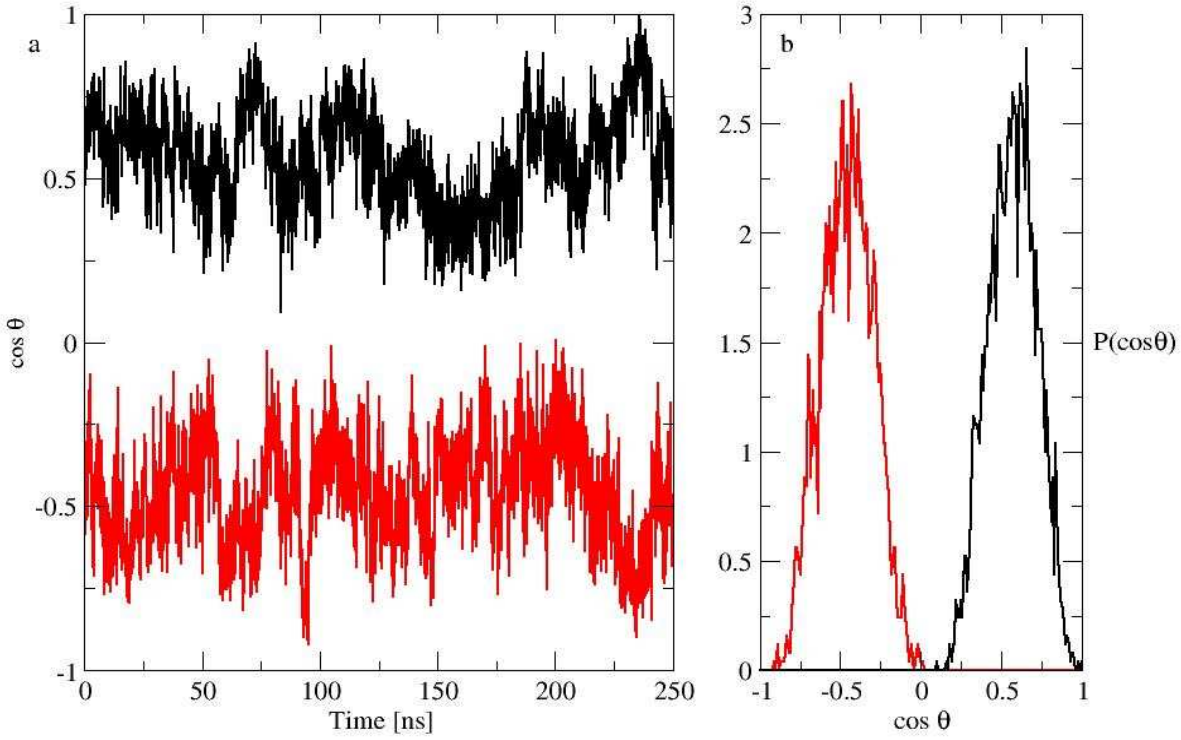

Figure S6: Alignment of FCP1 in the RAP74 binding pocket. **a)** Time traces of the cosine of the angles formed by the backbone dipole vectors of the FCP1 helix with the H2 helix (black curve) and the H3 helix (red curve). **b)** Probability distributions for the corresponding time traces. FCP1 tends to be partially aligned with the H2 helix and anti-aligned with the H3 helix.

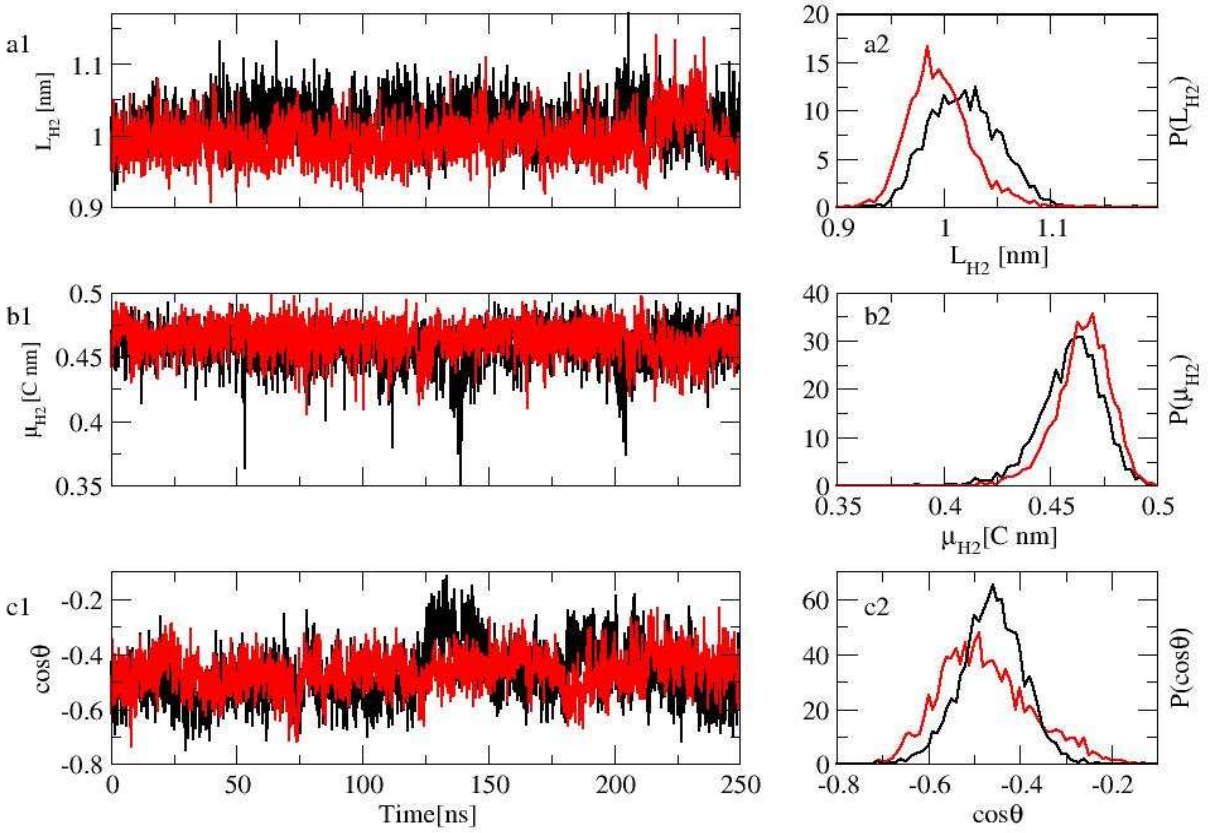

Figure S7: Characterization of RAP74 H2 in the apo and holo state. Column 1 presents time traces calculated from simulations of apo (black) and holo (red) RAP74 for **a1)** the H2 end-to-end distance; **b1)** the H2 backbone dipole moment; **c1)** the angle formed between the principal axes of H2 and H3. For each observable, column 2 presents corresponding distributions calculated from the time traces. The structure, fluctuations, and orientation of H2 remain relatively unchanged by the binding of FCP1.

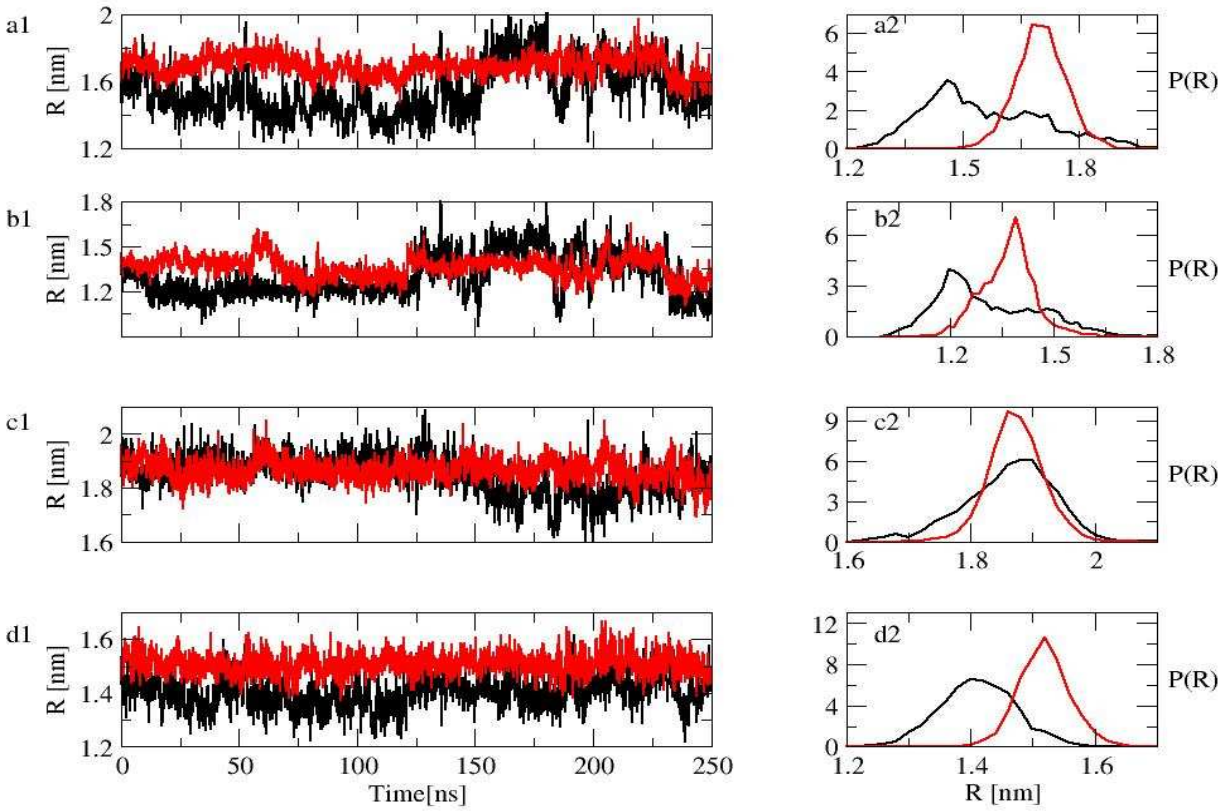

Figure S8: Packing of the RAP74 hydrophobic groove in the apo and holo state. Column 1 presents time traces calculated from simulations of apo (black) and holo (red) RAP74 for distances between **a1)** the N-termini of H2 (469) and H3 (485-486); **b1)** the C-terminal of H2 (475) and the N-terminal of H3 (485-486); **c1)** the C-termini of H2 (475) and H3 (500-501); **d1)** the N-terminal of H2 (469) and the C-terminal of H3 (500-501). Column 2 presents distribution functions calculated from the corresponding time traces. In each case, distances are calculated between the centers of mass defined by the alpha carbons of the indicated residues. The binding pocket appears to slightly open and become more stable upon binding FCP1.

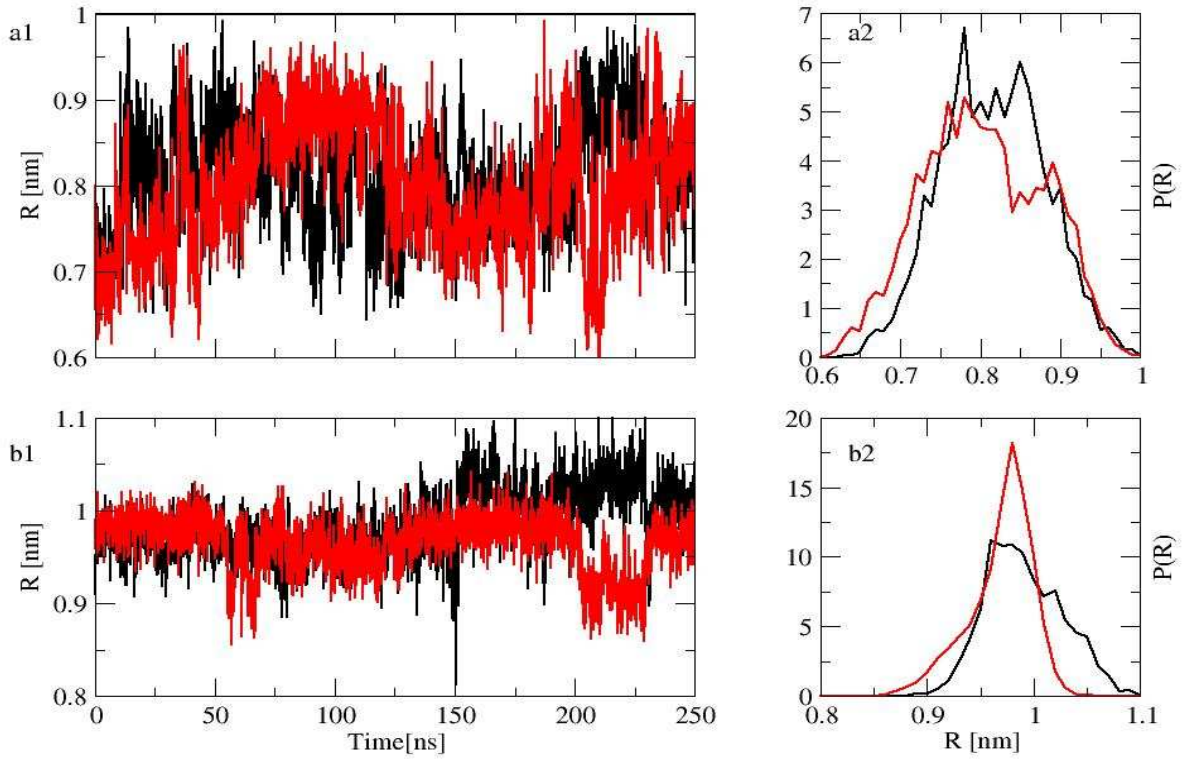

Figure S9: Changes in the location and fluctuations of RAP74 H2.5 in the apo and holo state. Column 1 presents time traces calculated from simulations of apo (black) and holo (red) RAP74 for distances between **a)** the C-terminal of H2 (475) helix and the N-terminal of H2.5 (478); and **b)** the C-terminal of H2.5 (483) and the N-terminal of H3 (485-486). Column 2 presents distribution functions calculated from the corresponding time traces. In each case, distances are calculated between the centers of mass defined by the alpha carbons of the indicated residues. Prior to binding FCP1, H2.5 samples conformations that are more distant from H3.

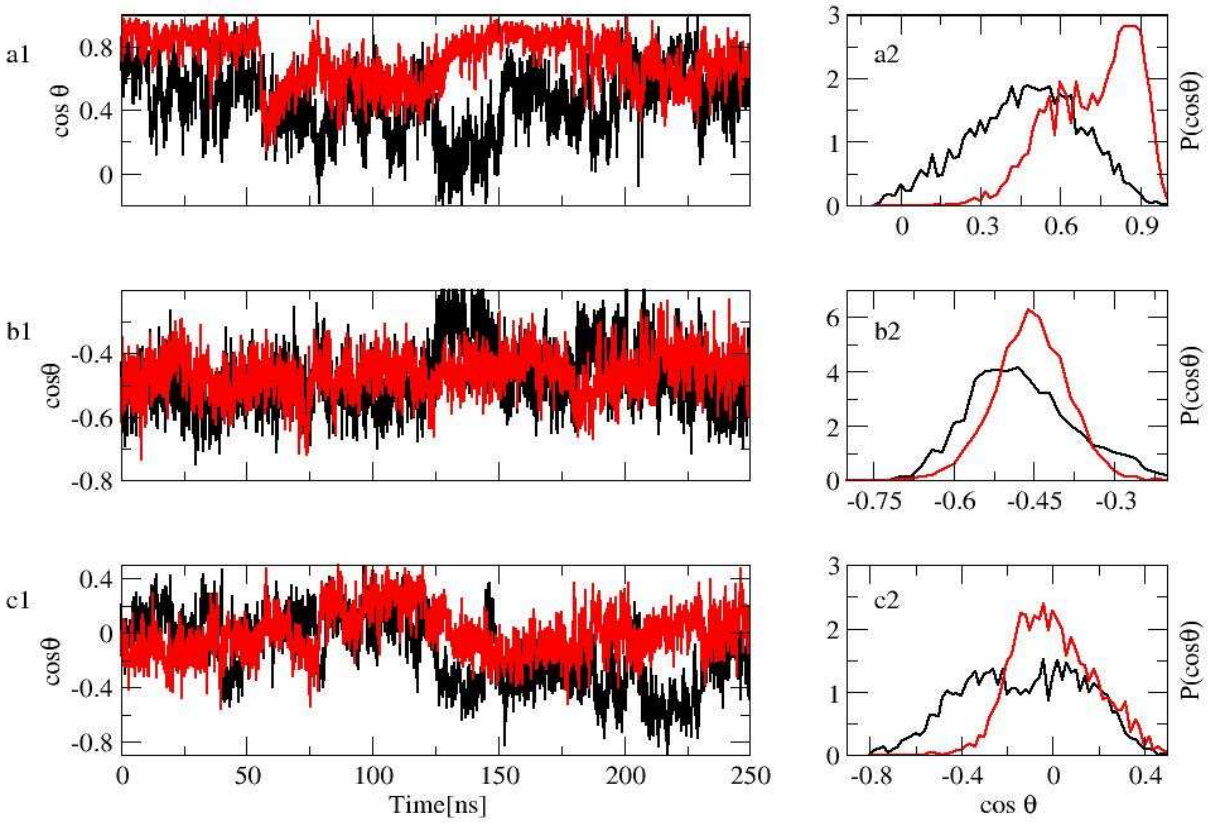

Figure S10: Orientation of RAP74 secondary structures in the apo and holo state. Column 1 presents time traces calculated from simulations of apo (black) and holo (red) RAP74 for the cosine of the angle formed by the principal axis vectors of **a1)** H2 and H2.5 helices; **b1)** H2 and H3 helices; **c1)** H2.5 and H3 helices. Column 2 presents distribution functions calculated from the corresponding time traces. Upon binding FCP1, H2.5 demonstrates increased tendency to align parallel with H2 and perpendicular with H3. In contrast, the angle formed by the axes of H2 and H3 appears unchanged.

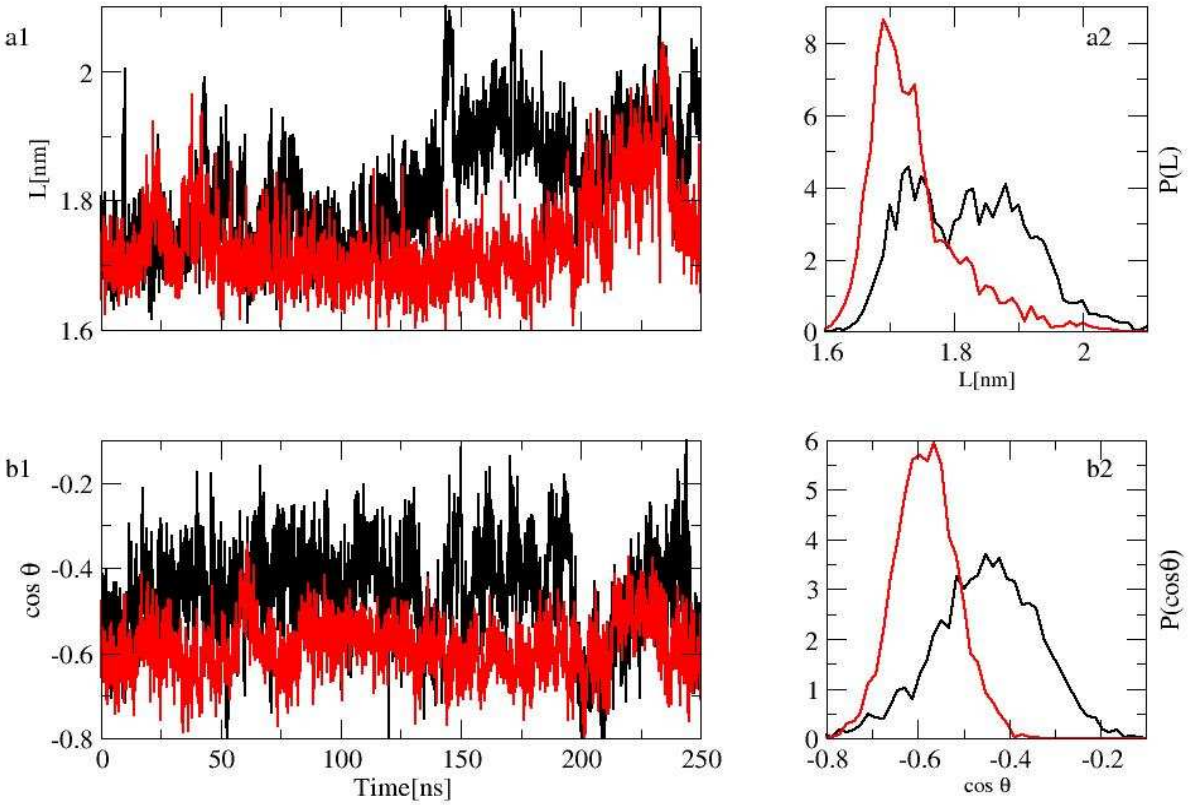

Figure S11: Changes in H1 structure and orientation resulting from binding FCP1. Column 1 presents time traces calculated from simulations of apo (black) and holo (red) RAP74 for **a1)** the H1 end-to-end distance (measured between the alpha carbons of residues 455 and 466); and **b1)** the cosine of the angle formed between the principal axes of H1 and H2. Column 2 presents distribution functions calculated from the corresponding time traces. Upon binding FCP1, H1 tends to adopt more compact conformation with a more antiparallel orientation with respect to the H2.

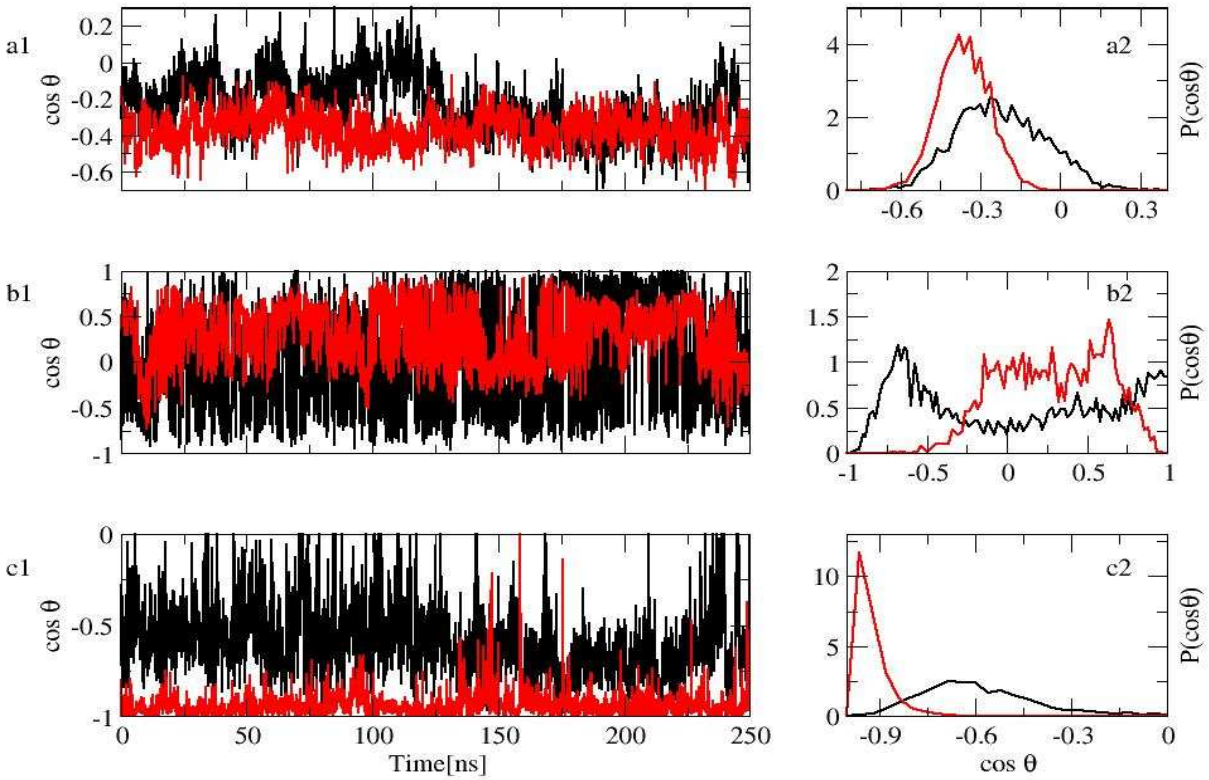

Figure S12: Orientation of secondary structures in RAP74 before and after binding FCP1. Column 1 presents time traces calculated from simulations of apo (black) and holo (red) RAP74 for the cosine of the angles formed by **a1)** the principal axes of H2 and S2; **b1)** the twist vectors of S1 and S2; **c1)** twist vectors of S1 and S3. Column 2 presents distribution functions calculated from the corresponding time traces. FCP1 stabilizes the alignment of S2 with respect to H2 and also dramatically rigidifies the interaction between S1 and S3.

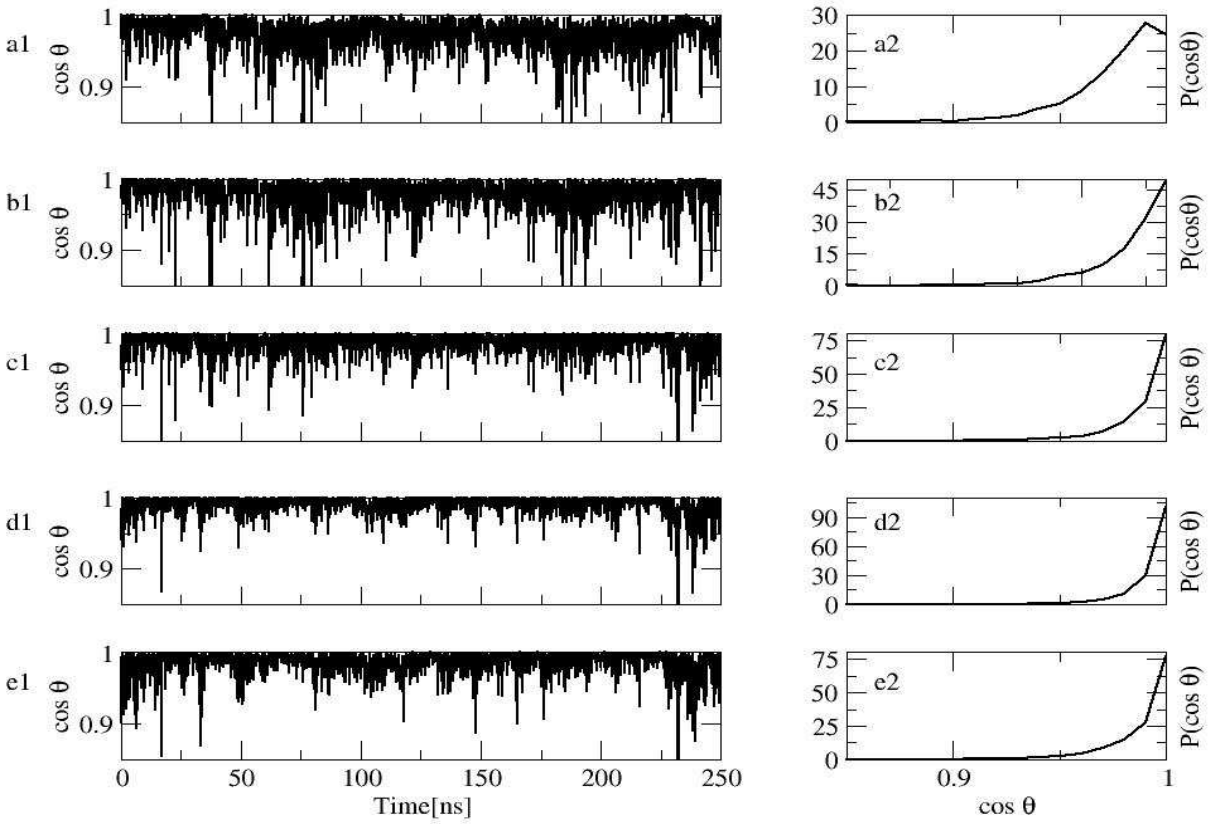

Figure S13: Angle of successive helix directors along the N-terminal region of FCP1. Column 1 presents time traces calculated from simulations of the RAP74-FCP1 complex for the cosine of the angle formed by the local helix directors at the i and i+4 alpha carbons of FCP1 including **a1)** Ser944 and Glu948; **b1)** Glu945 and Met949; **c1)** Ala946 and Ala950; **d1)** Asp947 and Lys951; and **e1)** Glu948 and Ala952. Column 2 presents distribution functions calculated from the corresponding time traces. The RAP74 binding pocket maintains the helical axis along the N-terminal of FCP1.

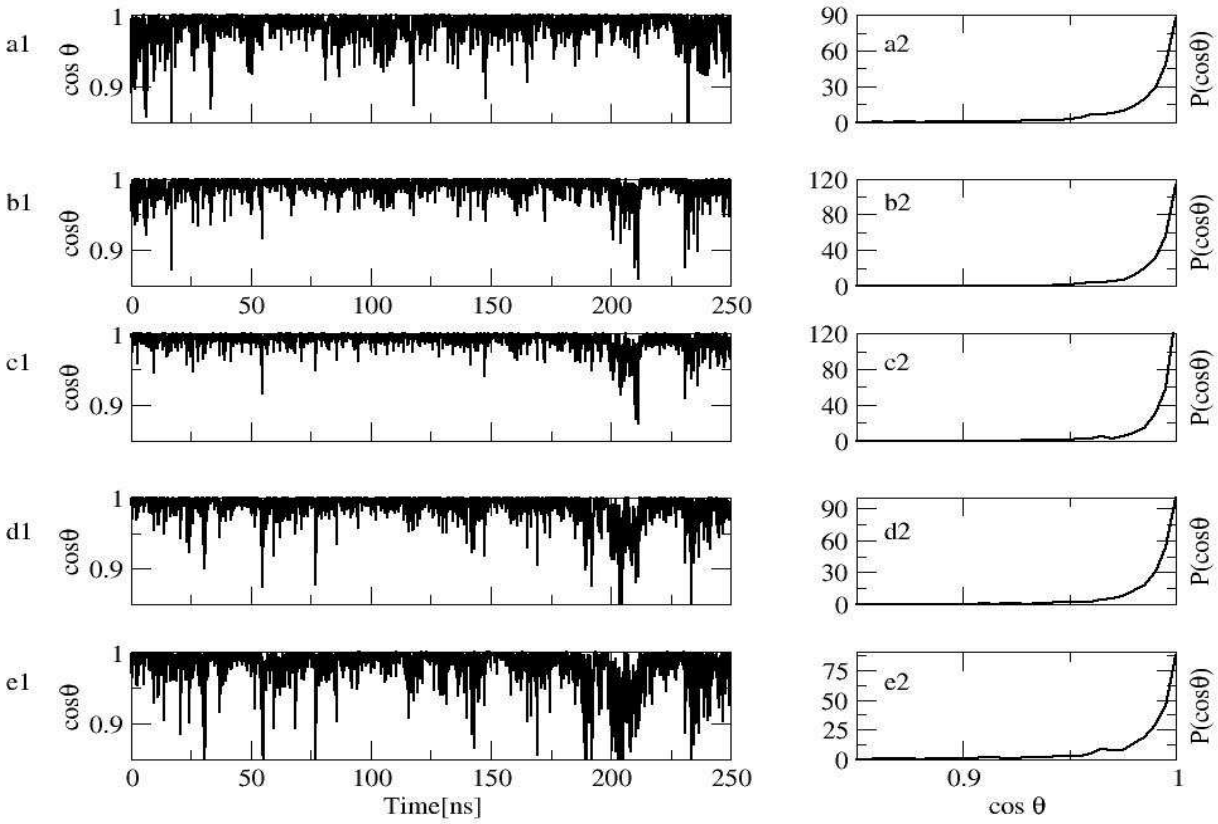

Figure S14: Angle of successive helix directors along the C-terminal region of FCP1. Column 1 presents time traces calculated from simulations of the RAP74-FCP1 complex for the cosine of the angle formed by the local helix directors at the i and i+4 alpha carbons of FCP1 including **a1)** Met949 and Leu953; **b1)** Ala950 and Glu954; **c1)** Lys951 and Ala955; **d1)** Ala952 and Glu956l; and **e1)** Leu953 and Leu957. Column 2 presents distribution functions calculated from the corresponding time traces. The RAP74 binding pocket maintains the helical axis of FCP1, although the C-terminal region samples somewhat larger and more correlated fluctuations than the N-terminal region.

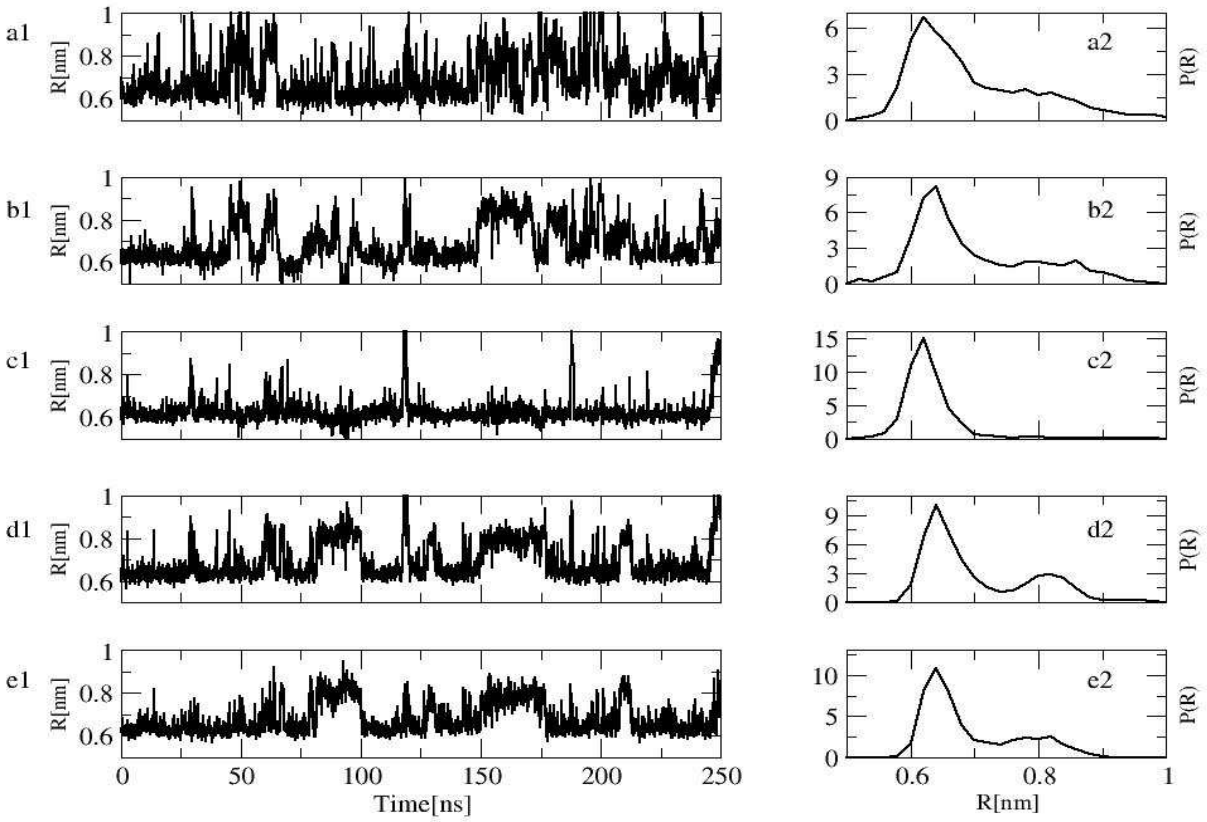

Figure S15: Distance between successive turns along the N-terminal of FCP1. Column 1 presents time traces calculated from simulations of the RAP74-FCP1 complex for the distances between i and i+4 alpha carbons of FCP1 including **a1)** Ser944 and Glu948; **b1)** Glu945 and Met949; **c1)** Ala946 and Ala950; **d1)** Asp947 and Lys951; and **e1)** Glu948 and Ala952. Column 2 presents distribution functions calculated from the corresponding time traces. Although the flanking Glu945-Met949, Asp947-Lys951, and Glu948-Ala952 pairs sample correlated fluctuations to larger distances, the Ala946-Ala950 pair samples much smaller fluctuations and appears to stabilize the N-terminal turn of FCP1 until the last ten nanoseconds of the simulation.

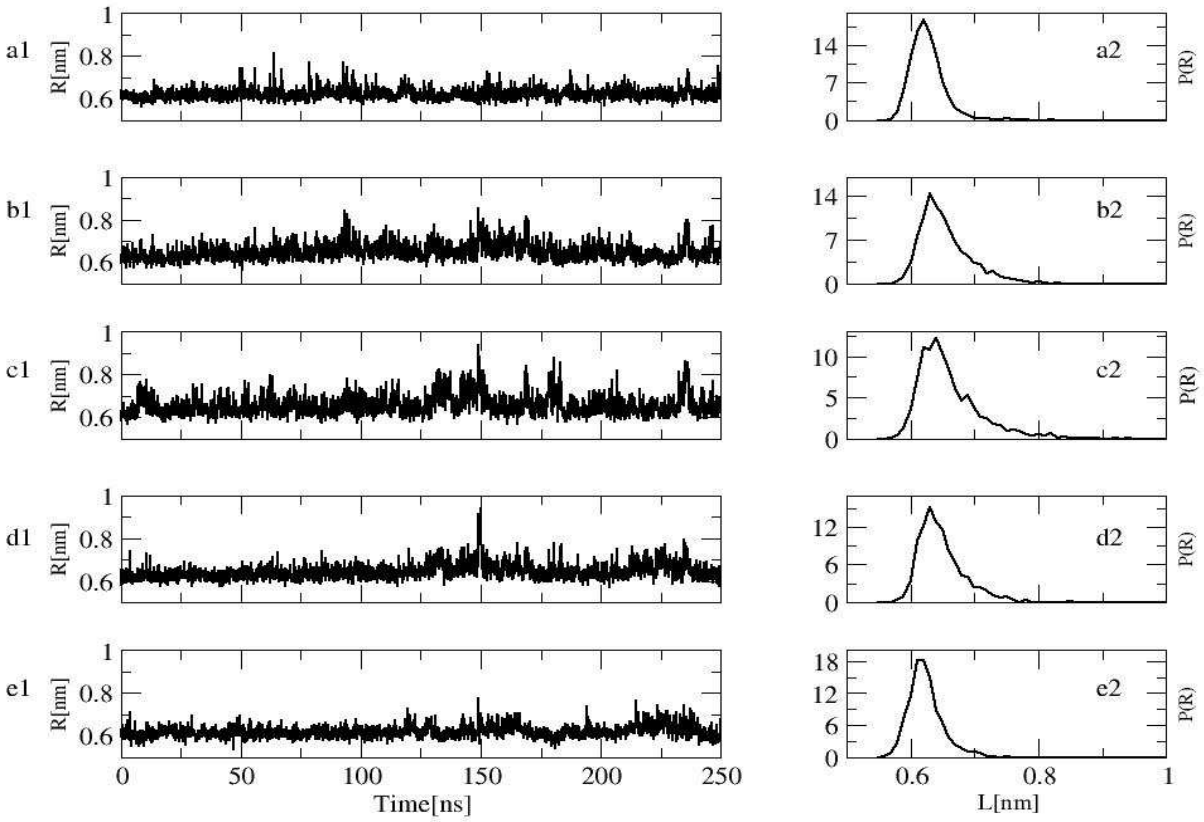

Figure S16: Distance between successive turns along the C-terminal of FCP1. Column 1 presents time traces calculated from simulations of the RAP74-FCP1 complex for the distances between i and i+4 alpha carbons of FCP1 including **a1)** Met949 and Leu953; **b1)** Ala950 and Glu954; **c1)** Lys951 and Ala955; **d1)** Ala952 and Glu956; and **e1)** Leu953 and Leu957. Column 2 presents distribution functions calculated from the corresponding time traces. The Met949-Leu953 and Leu953-Leu957 contacts remain very stable during the simulation and anchor the C-terminal turn of FCP1.

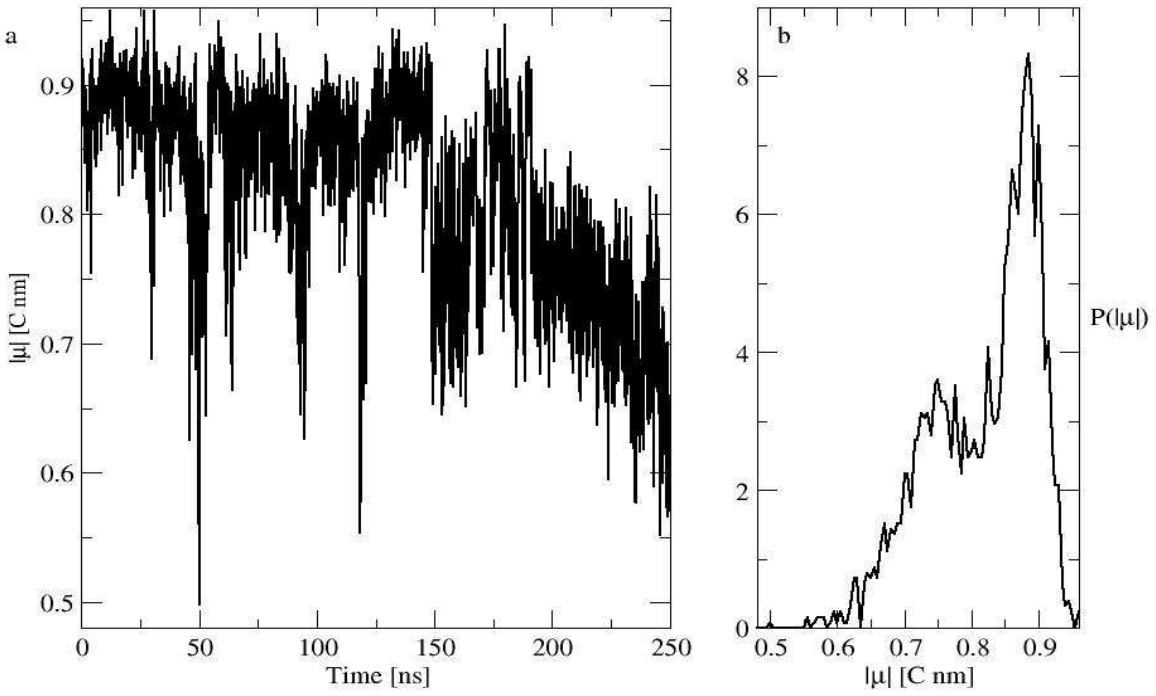

Figure S17: Dipole moment for the FCP1 backbone. Panel a presents the time trace calculated from simulations of the RAP74-FCP1 complex for the magnitude of the FCP1 backbone dipole. Panel b presents the corresponding distribution function. The FCP1 backbone dipole samples significant fluctuations and precipitously drops during the last 50 ns of the simulation.